Serb. Astron. J. № 211 (2025), 27 - 43 **UDC 524.354.4**
DOI: https://doi.org/10.2298/SAJ2511027G Original scientific paper

MULTI-FREQUENCY RADIO-CONTINUUM STUDY OF THE LMC SNR N206 (GOAT'S EYE) AND ITS "ZIG-ZAG" PWN

M. Ghavam[1], Z. J. Smeaton[1], M. D. Filipović[1], R. Z. E. Alsaberi[2,1], C. Bordiu[3], W. D. Cotton[4,5], E. J. Crawford[1], A. M. Hopkins[6], R. Kothes[7], S. Lazarević[1], D. Leahy[8], N. Rajabpour[1], S. Ranasinghe[8], G. P. Rowell[9], H. Sano[2], M. Sasaki[10], D. Shobhana[1], K. Tsuge[2,11], D. Urošević[12] and N. F. H. Tothill[1]

[1] *Western Sydney University, Locked Bag 1797, Penrith South DC, NSW 2751, Australia*
E–mail: *19594271@student.westernsydney.edu.au*

[2] *Faculty of Engineering, Gifu University, 1-1 Yanagido, Gifu 501-1193, Japan*

[3] *INAF-Osservatorio Astrofisico di Catania, Via Santa Sofía 78, I-95123 Catania, Italy*

[4] *National Radio Astronomy Observatory, 520 Edgemont Road, Charlottesville, VA 22903, USA*

[5] *South African Radio Astronomy Observatory Liesbeek House, River Park, Gloucester Road Cape Town, 7700, South Africa*

[6] *School of Mathematical and Physical Sciences, 12 Wally's Walk, Macquarie University, NSW 2109, Australia*

[7] *Dominion Radio Astrophysical Observatory, Herzberg Astronomy & Astrophysics, National Research Council Canada, P.O. Box 248, Penticton*

[8] *Department of Physics and Astronomy, University of Calgary, Calgary, Alberta, T2N IN4, Canada*

[9] *School of Physics, Chemistry and Earth Sciences, The University of Adelaide, Adelaide, 5005, Australia*

[10] *Dr Karl Remeis Observatory, Erlangen Centre for Astroparticle Physics, Friedrich-Alexander-Universität Erlangen-Nürnberg, Sternwartstraße 7, 96049 Bamberg, Germany*

[11] *Institute for Advanced Study, Gifu University, 1-1 Yanagido, Gifu 501-1193, Japan*

[12] *Department of Astronomy, Faculty of Mathematics, University of Belgrade, Studentski trg 16, 11000 Belgrade, Serbia*

(Received: July 16, 2025; Accepted: December 6, 2025)

SUMMARY: We present new radio-continuum observations of the Large Magellanic Cloud (LMC) supernova remnant (SNR) N206, which we give the name "Goat's Eye". Goat's Eye contains an interior radio structure that is likely a pulsar wind nebula (PWN), which we analyse in further detail. We use new radio observations from the Australia Telescope Compact Array (ATCA) telescope, as well as several archival radio observations, to calculate spectral indices, and find a steep spectral index for the whole SNR ($\alpha = -0.60 \pm 0.02$), and a flatter spectral index for the PWN ($\alpha = -0.16 \pm 0.03$). We also measure the polarisation and magnetic field properties of the PWN. Previously reported as a linear structure, the new observations show an unusual "zig-zag"-like structure, visible in radio-continuum total intensity, linear polarisation, and magnetic field orientations. The origin of this zig-zag structure is unclear, but we propose some origin scenarios that will require further observations to differentiate between.

Key words. ISM: supernova remnants – supernovae: general – supernovae: individual: N206 (Goat's Eye) – Radio continuum: general

1. INTRODUCTION

The Large Magellanic Cloud (LMC) is an irregular dwarf galaxy at a distance of 50 kpc from the Milky Way (MW)(Pietrzyński et al. 2019). The proximity and the low Galactic foreground absorption make the LMC an ideal laboratory for multi-frequency studies of supernova remnant (SNR) populations in great detail. Supernova (SN) explosions are important drivers of stellar and galaxy evolution, and SNRs are able to trace the interaction between the SN ejected material and the surrounding interstellar medium (ISM), revealing the relationship between SNR and galaxy evolution. SNRs in the LMC span a wide range of evolutionary phases, from young ejecta-dominated remnants, through middle-aged adiabatic remnants, to old remnants in the radiative phase.

Several surveys of the LMC SNR population have been conducted at multiple frequencies to study their overall physical properties (Filipovic et al. 1996, Filipović et al. 1998, Payne et al. 2007, 2008, Bozzetto et al. 2015, Maggi et al. 2016, Bozzetto et al. 2017, Leahy 2017, Filipović et al. 2021, Yew et al. 2021, Bozzetto et al. 2023, Filipović et al. 2021, Zangrandi et al. 2024). In particular, radio observations are particularly useful for studying individual SNRs, advancing our understanding of the underlying physics.

To further analyse the SNR population of the LMC, we present the study of the known SNR B0532−71.0 (Mathewson and Clarke 1973). This SNR is also known as SNR N206 (Klinger et al. 2002) and is located in the high-mass star-forming complex with the same name (also known as Henize 206, LHA 120-N 206, and DEM L221 Henize 1956), on the southern outskirts of the LMC. The region surrounds the star-forming cluster NGC 2018, also known as LHA 120-N 206A, and contains the HII region LHα 120-N206, with the SNR N206 located on the north-eastern edge (Gorjian et al. 2004). N206 has been examined across multiple wavelengths by various researchers (Mathewson and Clarke 1973, Lasker 1977, Milne et al. 1980, Mills et al. 1984, Williams et al. 1999, Klinger et al. 2002, Williams et al. 2005, Kavanagh et al. 2012).

The SNR N206 was initially discovered at radio frequencies (Mathewson and Clarke 1973), and has been analysed in several subsequent radio surveys, which show a bright source with a relatively flat spectrum (Milne et al. 1980, Mills et al. 1984); the most recent value showing $\alpha = -0.20 \pm 0.07$ (Klinger et al. 2002). The SNR has also been analysed in optical, which shows a circular edge-brightened filamentary shell (Lasker 1977, Long et al. 1981, Williams et al. 2005), and at X-ray frequencies which shows thermal X-ray emission filling the centre of the remnant (Williams et al. 1999, Williams et al. 2005, Kavanagh et al. 2012). This results in N206 being classified as a mixed-morphology (MM) SNR (Klinger et al. 2002, Williams et al. 2005) using the criteria of Rho and Petre (1998), and Williams et al. (2005) gives it an age of ∼25,000 years old, while Klinger et al. (2002) estimates an older age of ∼29,000 years, and Leahy (2017) gives an age of 13,000 years.

Australia Telescope Compact Array (ATCA) radio observations of Klinger et al. (2002) discovered a previously unseen linear radio feature on the east side of the remnant (Klinger et al. 2002). This feature was later detected in X-ray data from *Chandra* and *XMM-Newton*, showing associated X-ray emission with a small X-ray knot detected at the outer tip (Williams et al. 2005). This feature was classified as a pulsar wind nebula (PWN) (Klinger et al. 2002, Williams et al. 2005), but the associated pulsar was not detected in following dedicated Parkes observations (Williams et al. 2005).

The presence of this PWN classifies N206 as a composite SNR, a relatively rare class of SNRs within the Magellanic Clouds (MCs) with only a handful of such objects known. We know of three other confirmed composite SNRs within the LMC, 0453−6829 (Haberl et al. 2012, McEntaffer et al. 2012), 0540–69 (Brantseg et al. 2014), and 30 Dor B (Lazendic et al. 2000), as well as N49 (Ghavam et al. 2024), N59B (Bozzetto et al. 2012), and DEM L316B (Williams and Chu 2005) which are possible composite SNRs. We know of only two within the Small Magellanic Cloud (SMC), DEM S5 (Alsaberi et al. 2019) and IKT 16 (Owen et al. 2011, Maitra et al. 2015, 2021).

The modern generation of radio telescopes, such as MeerKAT and ASKAP, have allowed the discovery of several new SNRs and SNR candidates, both in our Galaxy (Kothes et al. 2017, Filipović et al. 2023, Burger-Scheidlin et al. 2024, Lazarević et al. 2024b, Smeaton et al. 2024b,a, Filipovic et al. 2025b) and in the MCs (Bozzetto et al. 2023, Cotton et al. 2024, Yew et al. 2021), as well as analyses which allow us to better understand the physical properties of already known SNRs (Filipović et al. 2024, Smeaton et al. 2025). The improved sensitivity and angular resolution also allow better analysis of a number of different astrophysical objects (Velović et al. 2022, 2023, Bordiu et al. 2024, Lazarević et al. 2024a, Asher et al. 2025, Bradley et al. 2025, Filipović et al. 2025a).

In this paper, we add to these analyses by presenting radio-continuum observations of the SNR N206, which we now give the nickname "Goat's Eye"[1]. The newly presented radio data come from the ATCA, MeerKAT, and Australian Square Kilometre Array Pathfinder (ASKAP) telescopes at frequencies ranging from 944 MHz to 9 GHz. The new high-resolution radio data shows more detail in the PWN, revealing a previously unseen "zig-zag" structure which we investigate further. We also present archival radio-continuum measurements from Murchison Widefield Array (MWA), Molonglo Observatory Synthesis Telescope (MOST), and combined ATCA and Parkes mo-

[1]The name "Goat's Eye" comes from the radio-continuum morphology which shows a circular shell with the bright linear PWN, which resembles a spherical eye with a large and unique horizontal/rectangular pupil as seen in goats.

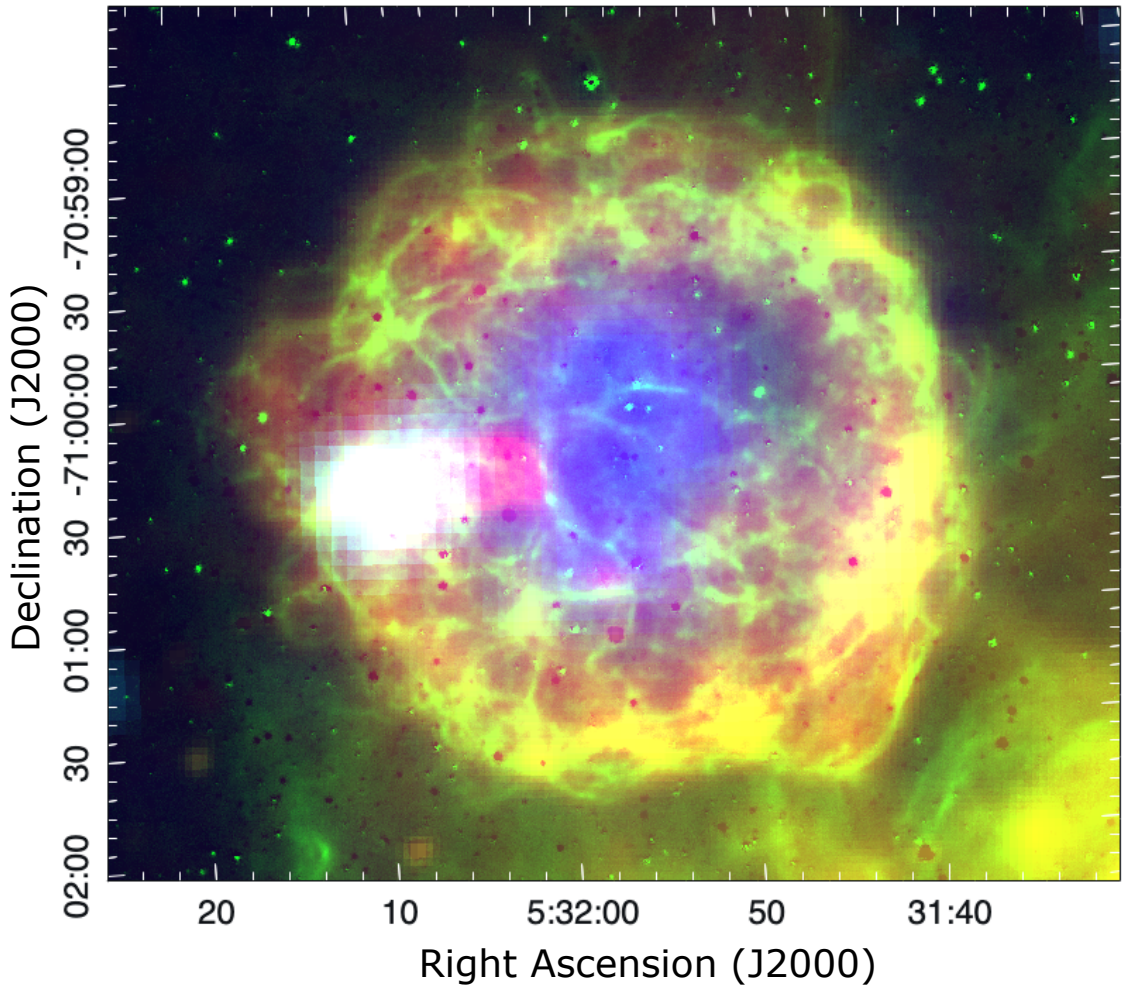

Fig. 1: Multi-frequency composite colour image of Goat's Eye. Red is radio-continuum MeerKAT data (1.3 GHz), green is optical DeMCELS [SII] data, blue is soft X-ray *XMM-Newton* data (0.2−1.0 keV), yellow is optical MCELS [OIII] data, and cyan is hard X-ray *XMM-Newton* data (2.0−4.5 keV). All images are linearly scaled.

saics, as well as previous optical and X-ray data to provide an overall multi-frequency view. We specifically analyse the properties of the linear PWN structure. In Section 2, we present the data used and observation details. In Section 3, we present the results and discussion, while in Section 4, we present our conclusions.

2. OBSERVATIONS AND DATA REDUCTION

2.1. Radio

2.1.1. ATCA data and processing

Here, we present details from our new ATCA observations at 5.5 and 9 GHz, which were acquired on 4$^{\rm th}$ December 2019 as part of project CX403. The observations were carried out using a 1.5C array configuration, with one hour of integration over a minimum 12-hour period. The observations used the Compact Array Broadband Backend (CABB) (with 2048 MHz bandwidth) at wavelengths of 3 and 6 cm (ν=4.5–6.5 and 8–10 GHz; centred at 5500 and 9000 MHz). We employed the standard southern-sky calibrator PKS B1934–638 for the primary (flux density) calibration, and source QSO J0047–7530 for the secondary (phase) calibration. Details of these calibrators can be found in the ATCA calibrator database[2]. The data contain both total power Stokes I observations and linear polarisation data, which are used in Section 3.5.

The data were reduced and analysed using MIRIAD (Sault et al. 1995) and KARMA (Gooch 1995) software packages. We produced and deconvolved images by setting the robust weighting parameter to 0.5 (for all 5.5 and 9 GHz images) and deconvolving via a primary beam correction. Both final Stokes I images achieve a resolution of 5″×5″ and a local Root Mean Squared (RMS) noise level

[2] https://www.narrabri.atnf.csiro.au/calibrators/calibrator_database.html

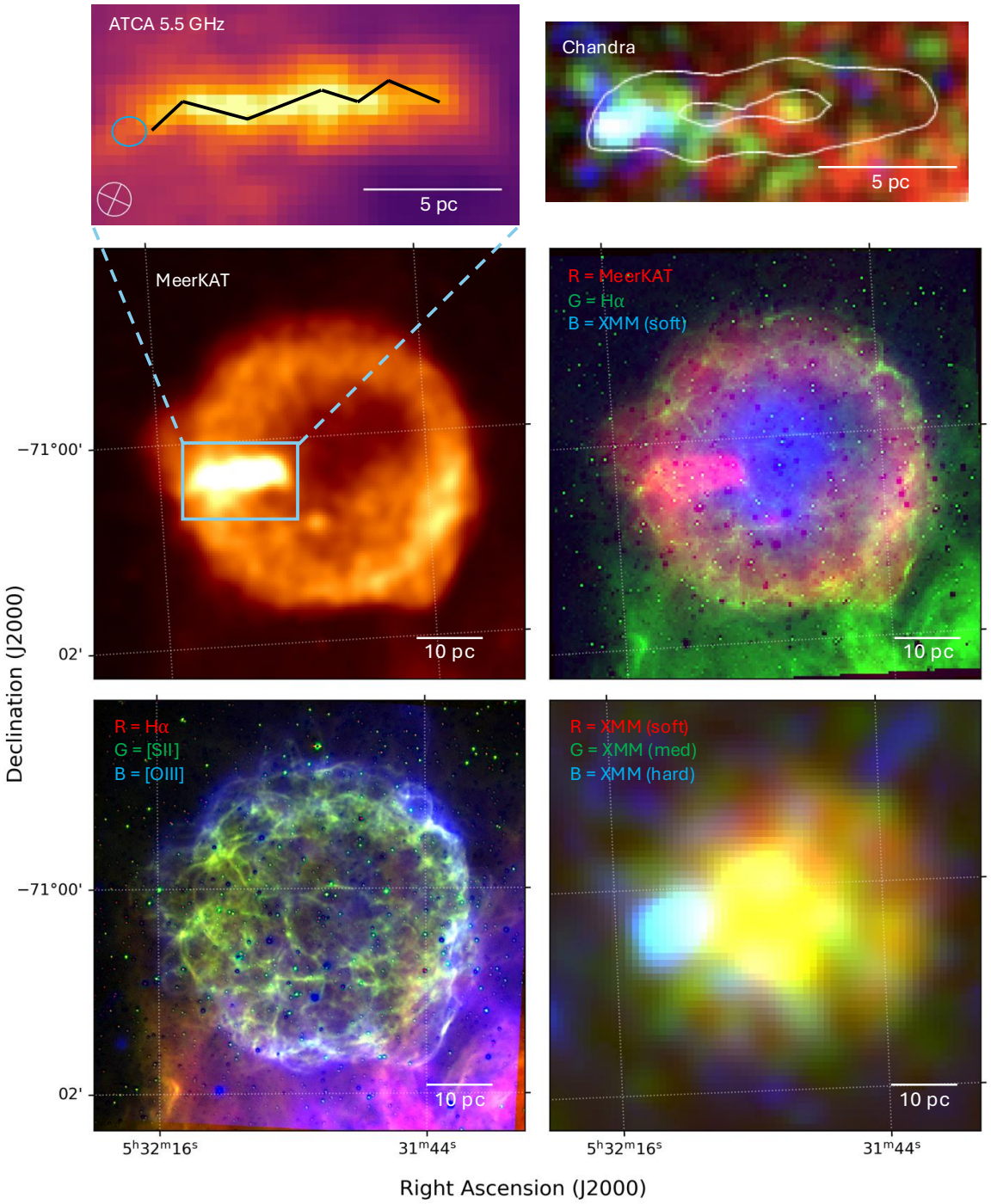

Fig. 2: 4-panel image of Goat's Eye. All images have linear scaling and display a relevant scale bar in the bottom right corner. **Top left:** MeerKAT radio-continuum image at 1.3 GHz. The left inset shows a zoomed-in ATCA 5.5 GHz view of the PWN. The described "zig-zag" structure is annotated with the black line and the position of the X-ray point source possible pulsar is shown in the blue circle. The beam size of $5'' \times 5''$ is shown in the bottom left corner. The top right image shows the same PWN view using an X-ray RGB made with *Chandra* data. Red is soft band (0.5−1.2 keV), green is medium band (1.2−2.0 keV), and blue is hard band (2.0−7.0 keV). Contours are from the left-hand ATCA image at levels of 0.4 and 0.8 mJy beam^{-1}. **Top right:** Multi-frequency RGB where red is MeerKAT radio at 1.3 GHz, green is DeMCELS Hα, and blue is *XMM–Newton* soft X-ray (0.2–1.0 keV). **Bottom left:** Optical RGB where red is DeMCELS Hα, green is DeMCELS [SII] and blue is MCELS [OIII]. **Bottom right:** *XMM–Newton* X-ray RGB where red is soft X-ray (0.2–1.0 keV), green is medium X-ray (1.0–2.0 kev), and blue is hard X-ray (2.0–4.5 keV).

of $\sim$14 μJy beam^{-1} for 5.5 GHz and $\sim$10 μJy beam^{-1} for 9 GHz.

We also used previous ATCA data in the form of archival mosaic images generated from combining ATCA and Parkes radio-continuum data for some flux density measurements (see Table 1). The properties and generation of these mosaics are described in further detail in Filipović et al. (1995, 1998), Dickel et al. (2005), Hughes et al. (2007), Filipović et al. (2021).

2.1.2. *Other radio data*

The MeerKAT data is obtained from the most recent LMC MeerKAT survey (project code SSV-20180505-FC-02). We make use of the broadband image from this dataset, centred at 1295 MHz over the bandwidth 856−1712 MHz (see Fig. 2, top left panel). Further image details, including calibration, data reduction, and the final survey information, will be presented in Cotton et al. (in prep) and Rajabpour et al. (in prep).

The ASKAP radio-continuum data primarily comes from the LMC survey conducted as part of the ASKAP commissioning and early science (ACES, project code AS033) (Pennock et al. 2021, Bozzetto et al. 2023). This observation was conducted using the entire 36-antenna array at 888 MHz with a 288 MHz bandwidth. The data has a restoring beam of 13.″9×12.″1 (position angle PA=–84.4°) and was reduced using the standard ASKAPSoft pipeline including multi-scale cleaning, self-calibration, and multi-frequency synthesis imaging (Guzman et al. 2019). We also use a 944 MHz flux density measurement from Smeaton et al. (in prep.), which was measured from the ASKAP Evolutionary Map of the Universe (EMU) survey data of the LMC (Hopkins et al. 2025).

We use radio-continuum data from the MWA (Tingay et al. 2013) GaLactic and Extragalactic All-Sky MWA (GLEAM) survey (Wayth et al. 2015, Hurley-Walker et al. 2017) of the LMC. We use the images at 118, 155, and 200 MHz as described in For et al. (2018) to measure the SNR flux densities.

We also use radio-continuum images from the Sydney University Molonglo Sky Survey (SUMSS) conducted with the MOST telescope to measure the flux density at 843 MHz. Details of this data and survey can be found in Mauch et al. (2003).

Archival HI data (Kim et al. 2003) were obtained using the ATCA and Parkes 64-m telescope. The angular resolution of the data is 60″, corresponding to a spatial resolution of $\sim$15 pc at the distance of the LMC (Pietrzyński et al. 2019). The typical noise level is $\sim$2.4 K at a velocity resolution of 1.689 km s^{-1}.

2.2. Optical

The optical data shown is from the Magellanic Cloud Emission Line Survey (MCELS) and DeMCELS optical surveys (Smith and MCELS Team 1999, Points et al. 2024), which imaged the LMC using the UM/CTIO Curtis Schmidt telescope. The DeMCELS survey achieves a higher resolution, but does not include images using the [OIII] filter. Therefore, the images used are the Hα and [SII] images from the DeMCELS survey, and the [OIII] image from the MCELS survey (see Fig. 2, bottom left panel).

2.3. X-Ray

The X-ray data shown are from the *XMM-Newton* telescope survey of the MCs (Haberl 2014, Maggi et al. 2016, 2019), and from the *Chandra* telescope. The *XMM* survey used a bandwidth 0.2−10.0 keV and achieved a sensitivity of $F_{\rm X}$ (0.3−8 keV) $\approx 10^{-14}$ erg cm^{-2} s^{-1}. We show all three X-ray bands, soft, medium, and hard (see Fig. 2, bottom right panel). The *Chandra* data achieves a higher resolution but a lower sensitivity than *XMM-Newton*, and is therefore less sensitive to the more diffuse shell structure. While the shell is visible in the soft *Chandra* band, this diffuse emission is better seen in the *XMM-Newton* data, and the *Chandra* data is primarily used to analyse the PWN with higher resolution and specifically show the X-ray point source (see Fig. 2, top right inset). We use all three *Chandra* bands, soft (0.5−1.2 keV), medium (1.2−2.0 keV), and hard (2.0−7.0 keV), and the images were generated by merging together two separate *Chandra* observations at each band.

3. RESULTS AND DISCUSSIONS

3.1. Morphology

3.1.1. *Goat's Eye Shell*

The radio-continuum images show a circular, edge-brightened, shell-type morphology (see Fig. 2, top left panel) with the bright linear radio feature identified by Klinger et al. (2002) in the eastern side. There are also two areas, on the east and south-west of the SNR, which deviate slightly from this circular shape. These areas are potentially small blowout structures, sometimes referred to as "ears" (Chiotellis et al. 2021), as seen in some other SNRs (e.g. G1.9+0.3 (Luken et al. 2020), SNR S147 (Xiao et al. 2008), SNR J0455−6838 (Crawford et al. 2008)). The edge-brightened shell is fairly symmetrical, with the exception of the brighter south-west rim.

From the MeerKAT data, we measure the SNR by eye, and find a geometric centre to be at RA(J2000) = 05:31:56.6, Dec(J2000) = −71:00:17, with an angular size of 3.′0×3.′1, corresponding to a physical size of 44 pc×45 pc at the LMC distance of 50 kpc (Pietrzyński et al. 2019). This is slightly smaller than that reported in Klinger et al. (2002) from their ATCA data (44 pc×47 pc), however this is likely due to fitting the region by eye as exact region parameters were not previously reported. This physical size is slightly larger than the average diameter for the LMC population (mean diameter of 41 pc for

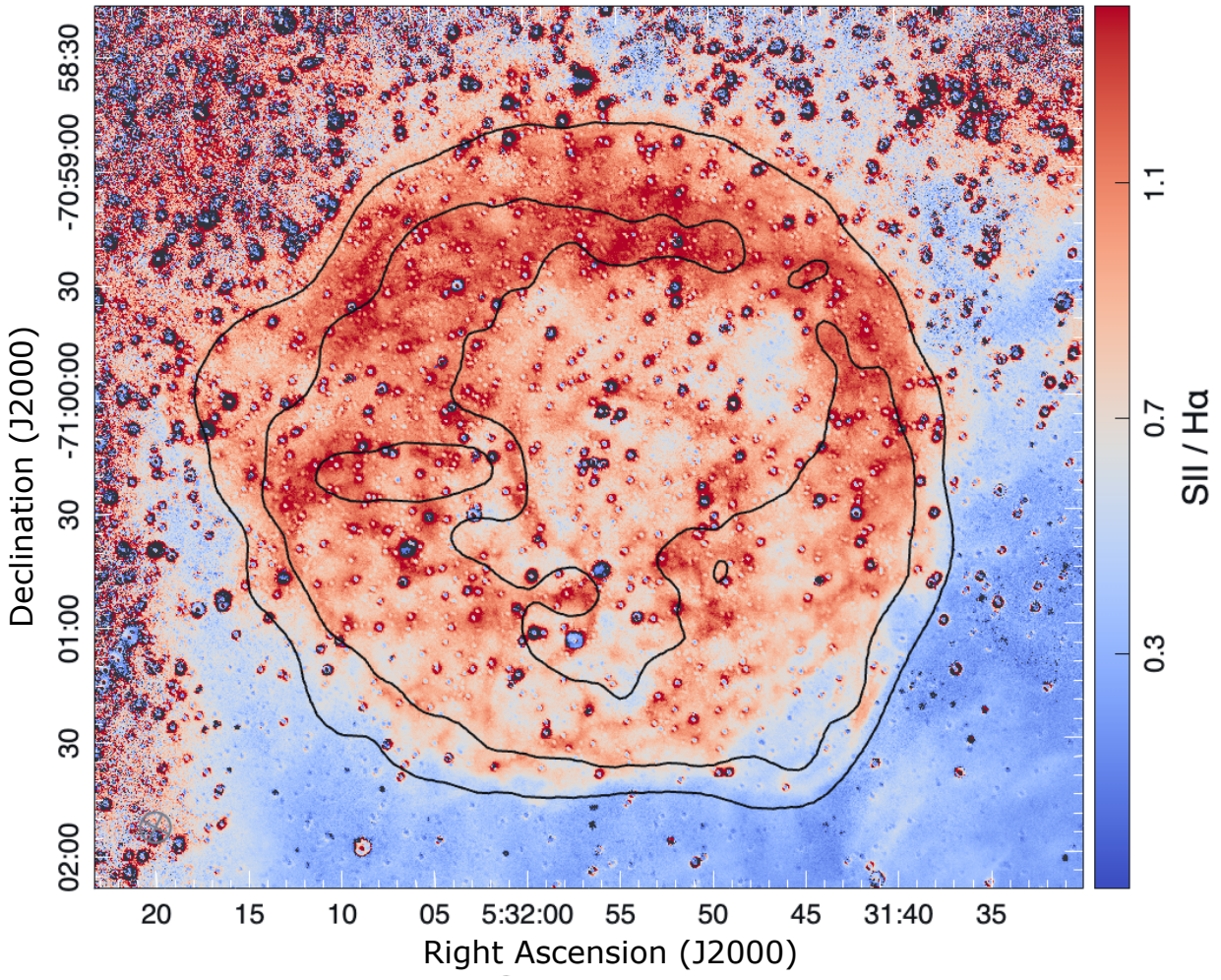

Fig. 3: [SII]/Hα ratio map of Goat's Eye from optical DeMCELS data. The contours are from the MeerKAT radio-continuum image at levels of 0.3, 0.8, and 2.0 mJy beam^{-1}.

the LMC; Bozzetto et al. 2017), but still well within the population distribution for an SNR.

Goat's Eye also has an observed optical shell, with an inner filamentary structure seen in Hα and [SII], and an outer [OIII] rim. We detect bright interior thermal X-ray emission in the soft X-ray band, but do not detect the outer shell. The spatial structure of the [SII]/Hα shell closely matches the radio-continuum shell in the MeerKAT image, with the [OIII] extending slightly beyond this emission. This [SII] emission extends across the entire SNR and matches the radio-continuum extent, indicating that the shock-wave is composed of predominantly radiative shocks. The two potential blowout regions seen in the radio-continuum images are also seen in Hα and [SII], indicating that they are components of the expanding shell structure. The Hα and [SII] emission shows a filamentary web-like structure over the SNR, which may be indicative of expansion into a porous ISM (Dimaratos et al. 2015).

Such filamentary optical structures are not unusual in SNRs, such as 0450−7050 (Smeaton et al. 2025). The point that makes Goat's Eye's morphology so unusual is the [OIII] emission being located outside of the [SII]/Hα shell, as it is typically located closer to the interior where the temperature is often higher, or at areas of faster shock velocities where significant interaction may be occurring. The fact that we see an [OIII] shell around the entire SNR leading the slower, radiative shell seen in [SII] and Hα indicates there may be a complex velocity structure in the shell. If the SN occurred in a cavity which was cleared by the progenitor wind, then this may help to explain the observed properties. The [OIII] may indicate the point where the shock is just reaching the end of the cavity and is hitting the cavity walls with sufficient velocity to emit [OIII] emission. This may also help to explain the extremely filamentary structure visible in [SII] and Hα, since the pre-excavated cavity could have created a complex, porous density structure resulting in the filamentary structure as the shock waves preferentially expand into the lowest density paths.

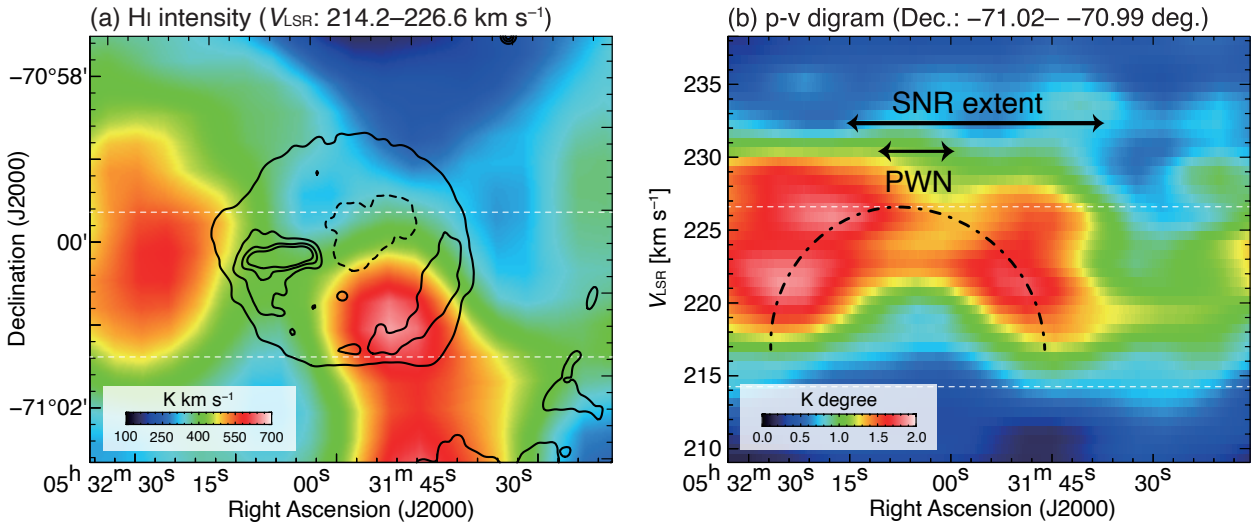

Fig. 4: HI integrated intensity map and $p-v$ diagram of Goat's Eye and surrounding environment. **Panel (a):** HI intensity map of Goat's Eye and surrounding environment integrated over the $V_{\rm LSR}$ velocity range of 214.2–226.6 km s^{-1}. Black contours are from MeerKAT 1.3 GHz radio-continuum map at levels of 0.5, 1.0, 1.5, and 2.0 mJy beam^{-1}. The dashed white horizontal lines correspond with panel (b) and show the extent of the possible HI cavity. **Panel (b):** HI p–v diagram, integrated over Goat's Eye's Dec location (−71.°02– −70.°99). The dashed white horizontal lines correspond with panel (a) showing the location of the cavity relative to Goat's Eye. The black dashed arc traces the possible HI cavity, and the labelled arrows display the PWN and SNR physical extents.

There is also a thick shell observed in radio, approximately 30″ inward for the thickest shell. There are multiple possible reasons for this thicker shell. Potentially, as the expanding shock wave is encountering the cavity wall, it begins to bounce back and slow down, travelling back toward the SNR interior. However, with lower shock velocities as demonstrated by the [SII]/Hα correlation. This material would then be compressed on both sides, and thus could be stacked up and form a thick inner shell. Additionally, as it expands inwards, it will encounter the SN ejecta, which may result in enhanced mixing and cause a turbulent zone inside the outer shell.

In Fig. 3, we display the [SII]/Hα ratio map generated from the optical DeMCELS data. We measure an average of ∼1.1±0.4 over the entire shell, with higher values of ∼1.2−1.3 in the northern half. This suggests that the northern shock may have slowed down and is becoming radiative, or has enhanced cooling in this region (see also Reid et al. 2015, Bozzetto and Filipović 2014). The southern shock, oriented toward the HII region, shows radio edge brightening, indicating potential interaction.

We also checked the available Infrared (IR) *Herschel* and *Spitzer* images of the LMC (Meixner et al. 2013), and do not see Goat's Eye's shell visible. This is expected from the results of Lakićević et al. (2015), who found no significant dust heating or interaction in their IR analysis. Therefore, if there is interaction between the SNR shell and the nearby HII region, it may be just beginning, or if the shocks are particularly slow, then they may not be energetic enough to cause significant dust heating. Alternatively, the SNR and the HII region may be separated by an offset along the line of sight, which would explain the lack of observed interaction.

3.1.2. Shell Symmetry

To quantify the Goat's Eye's shell symmetry, we measure the multipole values from the MeerKAT radio-continuum images and compare with the results of Ranasinghe and Leahy (2019) and Leahy et al. (2025). Using the method of Ranasinghe and Leahy (2019) we measure values of $P_2/P_0 = 280.23\pm0.51\times10^{-6}$ and $P_3/P_0 = 16.596\pm0.063\times10^{-6}$, which place Goat's Eye in the centre of the SNR population studied in Ranasinghe and Leahy (2019). Therefore, this comparison is not definitive in classifying Goat's Eye's morphology.

Following the newer method of Leahy et al. (2025), we calculate the radial and angular dipoles, quadrupoles, and octopoles separately. We find that Goat's Eye's radial component has a low dipole moment and is dominated by the quadrupole moment, and the angular component is dominated by the dipole moment. This matches the radio morphology displayed in Fig. 2, where the main deviation in radial asymmetry is caused by the two small blowout structures seen in the south-west and north-east. These structures are resulting in two directions of asymmetry, and thus a larger quadrupole moment. The higher angular dipole moment is likely being caused by the bright PWN in the east, and thus this indicates that this is the dominant cause of angular asym-

metry in Goat's Eye. Leahy et al. (2025) primarily used X-ray morphologies, and we note that the radio multipoles are significantly different from the X-ray multipoles reported for Goat's Eye, indicating that there are significant differences in the radio and X-ray morphology, as observed in our images (see Fig. 2).

This low radial dipole moment, and the observed radio morphology, show a remarkably circular structure, similar to some of the most circular SNRs, such as the Galactic SNR Teleios (Filipovic et al. 2025b) and the circumgalactic SNR J0624−6948 (Filipović et al. 2022, Sasaki et al. 2025). For such an evolved (Klinger et al. 2002, Williams et al. 2005, ∼25,000−29,000 years) core-collapse (CC) SNR, this remarkable circularity is unusual. Goat's Eye undoubtedly originates from a CC SN due to the presence of the PWN. CC SNs are expected to have asymmetrical explosions (Lopez et al. 2009, 2011), and thus asymmetrical remnants, as opposed to their more symmetrical Type Ia counterparts. However, this possible correlation is debated in the literature (Ranasinghe and Leahy 2019, Leahy et al. 2025). Additionally, SNRs are expected to remain more circular when they expand into more rarefied and homogeneous environments, for example, in the cases of Teleios and J0624−6948. The nearby HII star-forming region to the south-west makes this scenario less likely for Goat's Eye, however it is possible that there is an offset between Goat's Eye and the HII region which would account for the lack of interaction signatures. If Goat's Eye is in close physical proximity to the neighbouring region, then it is unusual that Goat's Eye was able to retain such a circular shape throughout its evolution, and this would require detailed modelling that accounts for the complex environment and explosion subtype.

3.1.3. Goat's Eye's PWN

The finer structure of the PWN feature is shown in the higher-resolution ATCA data (see Fig. 2, inset), with a measured length of 50″, corresponding to a physical length of ∼12 pc for the LMC. Originally described as a linear feature in Klinger et al. (2002), the new ATCA observations show a more "zig-zag"-like structure. This proposed structure is highlighted in the inset image by the annotated black line. There is also a bright, non-thermal, X-ray point source located at the east side of the PWN, reported in Williams et al. (2005). This source is visible in the *Chandra* X-ray images (see Fig. 2, top right inset), and is clearly located within the bounds of the PWN as shown by the radio contour levels. There is no corresponding radio point source visible.

This structure was suggested to be a run-away, or bow-shock, PWN (Klinger et al. 2002), wherein a pulsar is given a high kick velocity during the initial SN explosion. This runaway pulsar then travels supersonically, generating a tail trailing behind which can emit strongly at X-ray and radio frequencies. This scenario was explored in more detail in Klinger et al. (2002). The morphology of Goat's Eye's PWN supports this scenario as it shows similarities to other known bow-shock PWN, such as DEM S5 in the SMC (Alsaberi et al. 2019), the Galactic Lighthouse PWN (IGR J11014-6103 Pavan et al. 2014b,a, 2016), the Galactic Potoroo PWN (Lazarević et al. 2024a), and the Galactic Mouse PWN (Yusef-Zadeh and Bally 1987, Camilo et al. 2002). Goat's Eye appears to be particularly similar to the Galactic Mouse PWN, which also appears to be moving away from the centre of a nearby SNR G359.1−0.5. Recent results however, argue that the Mouse PWN is not physically associated with G359.1−0.5 as the pulsar is moving too slowly and thus is too old to have originated from the SNR (Hales et al. 2009).

In the case of Goat's Eye's bow-shock PWN, the head of the bow-shock structure would contain the high-velocity pulsar, on the eastern side travelling out of the SNR, and the tail pointing back toward the geometric centre of the PWN; the origin point of the pulsar. An X-ray point source is detected on the eastern side of the PWN (Williams et al. 2005), which may represent the pulsar. This is unconfirmed however, as previous timing searches did not detect the presence of a pulsar (Williams et al. 2005). We do not detect any radio counterpart to this source, or detect any compact radio sources within the PWN. It is possible that the pulsar is present, but radio quiet, or that the presence of the pulsar is hidden within the PWN emission. Klinger et al. (2002) estimated a tangential velocity of ∼800 km s^{-1}, which is a reasonable velocity value for a bow-shock PWN, and thus the Goat's Eye pulsar may have been born at the time of the SN explosion and be physically associated.

3.1.4. Distribution of HI *clouds*

The spatial distribution of HI emission toward Goat's Eye is presented in Fig. 4 (panel a). An HI cloud is identified in the south-western part of the remnant, coinciding with a region of enhanced radio continuum emission. Another HI structure is observed along the eastern shell. In contrast, there is less HI emission visible in the north-western region. This lower emission corresponds with a more circular shell structure with lower radio-continuum emission. This supports the scenario that the enhanced radio-continuum emission and slight asymmetries are due to interaction with neighbouring HI regions which is not present in this area.

Fig. 4 (Panel b) shows the position–velocity ($p-v$) diagram of HI emission toward Goat's Eye. There is a possible arc-like feature which appears to trace the peaks of HI in the $p-v$ diagram. This possible feature spans a spatial diameter of 44 pc and has a velocity width of ∼10 km s^{-1}. While the extent of the radio shell does not fully coincide with this possible HI structure, it appears that the geometric centre of the expanding HI shell potentially aligns with the spatial position of the PWN.

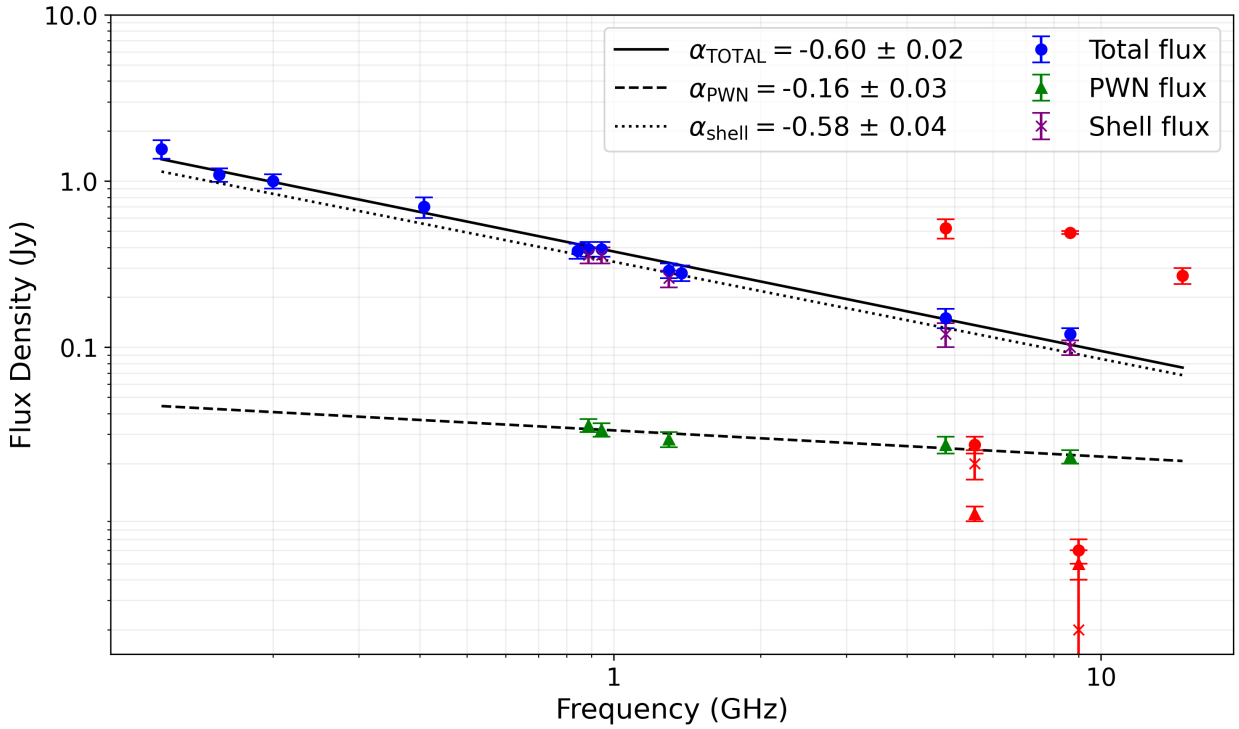

Fig. 5: Radio-continuum spectrum of Goat's Eye using radio-continuum data from (Table 1). The black solid line gives the total spectral index, the black dashed line gives the PWN spectral index, and the black dotted line gives the shell spectral index, as shown in the legend. The points in red are the non-fitted data in Table 1.

Given the low angular resolution of the HI data (60″) it is difficult to determine if this is a true alignment. The angular size of the shell is ∼3′, approximately 3 times the HI angular resolution, and the PWN is ∼ 1′. Therefore, the large-scale HI distribution is likely reliable, but the smaller-scale features related to the PWN are less definitive as they are at the same spatial scale as the HI resolution. It is possible that the larger-scale structure was formed by stellar winds from a massive progenitor. If this is the case, then it is supported by the measured velocity width of ∼10 km s^{-1}, which is reasonable for these kinds of structures (Sano et al. 2021, 2022, Fukui et al. 2024).

3.2. Flux density

We measure the flux density of both the entire SNR from all available radio frequencies, and of the PWN for data with sufficiently good resolution. We also subtracted the nearby background emission when measuring flux density, as explained in Hurley-Walker et al. (2019). This process was done by fitting a circular region around the entire shell and an elliptical region around the PWN using the astronomy imaging software Cube Analysis and Rendering Tool for Astronomy (CARTA) (Comrie et al. 2018). These same regions are used for all the flux density measurements shown in Table 1. The errors are taken as 10% following a similar process to that used in Filipović et al. (2022, 2023, 2024), Smeaton et al. (2024a), Bradley et al. (2025), and Alsaberi et al. (2025). We also calculate the flux density of the shell by taking it as the difference between the total and PWN flux densities.

3.3. Spectral Index

We use the flux density measurements shown in Table 1 to calculate the spectral index of Goat's Eye, where the spectral index is defined as $S \propto \nu^{\alpha}$ (Filipović and Tothill 2021). We calculate the spectral index separately for both the total SNR and for the PWN (see Fig. 5). The fitting is done using the LINREGRESS[3] function from the SCIPY Python library (Virtanen et al. 2020).

Initially, all radio-continuum data points were used for the fitting, and there were some points that were significant outliers to the fit. To quantify this, we measured the reduced χ^2 value as the sum of (residuals/rms)^2, where residuals = measured value − model value. We calculate a reduced χ^2 value of 60.37 for the fit. The main outliers were the ATCA data points; the 4798 and 8638 MHz data points from Klinger et al. (2002) were much higher than the fit, and the 5500 and 9000 MHz data measured in this

[3] https://docs.scipy.org/doc/scipy/reference/generated/scipy.stats.linregress.html

Table 1: Flux density measurements of Goat's Eye at multiple radio frequencies. ⋆ indicates that a quoted uncertainty was not given. † indicates flux density measurements which are included in the table, but which were not used in the spectral index estimate, see text for details.

ν (MHz)	$S_{\rm Total}$ (Jy)	$S_{\rm PWN}$ (Jy)	$S_{\rm Shell}$ (Jy)	Telescope	Reference
118	1.56±0.2	–	–	MWA	This work (from For et al. (2018) image)
155	1.09±0.1	–	–	MWA	This work (from For et al. (2018) image)
200	1.00±0.10	–	–	MWA	This work (from For et al. (2018) image)
408	0.7±−⋆	–	–	MOST	Mathewson and Clarke (1973)
843	0.38±0.04	–	–	MOST	This work (from Mauch et al. (2003) image)
888	0.39±0.04	0.034±0.003	0.36±0.04	ASKAP	This work (from Pennock et al. (2021) image)
944	0.39±0.04	0.032±0.003	0.36±0.04	ASKAP	Smeaton et al. (in prep)
1298	0.29±0.03	0.028±0.003	0.26±0.03	MeerKAT	This work (from Cotton et al. (in prep) image
1377	0.28±0.03	–	–	ATCA + Parkes	This work (from Hughes et al. (2007) image)
4798	0.52±0.07†	–	–	ATCA	Klinger et al. (2002)
4800	0.15±0.02	0.026±0.003	0.12±0.02	ATCA + Parkes	This work (from Dickel et al. (2005) image)
5500	0.030±0.003†	0.010±0.001†	0.020±0.004	ATCA	This work
8638	0.49±0.12†	–	–	ATCA	Klinger et al. (2002)
8640	0.12±0.01	0.022±0.002	0.10±0.01	ATCA + Parkes	This work (from Dickel et al. (2005) image)
9000	0.007±0.001†	0.005±0.001†	0.002±0.002	ATCA	This work
14700	0.27± −⋆ †	–	–	Parkes	Milne et al. (1980)
	$\alpha_{\rm Total}$	$\alpha_{\rm PWN}$	$\alpha_{\rm Shell}$		
	-0.60 ± 0.02	-0.16 ± 0.03	-0.58±0.04		

research (project CX403) were much lower. We investigated our ATCA data and found that there were significant missing short spaces, which are likely resulting in a flux density underestimation. To mitigate this, we searched the mosaic images of Dickel et al. (2005), which combines the ATCA interferometry data with single-dish Parkes data to fill in the missing short spacings. We found merged images at 4800 and 8640 MHz, which are similar frequencies to the outlying points. These new points fit the line much better and thus are used instead of the ATCA outlying points. We also exclude the 14700 MHz data point from Milne et al. (1980), as it is also an outlier, likely due to lower sensitivity and resolution from the older survey. After excluding these points, we achieve a reduced χ^2 value of 0.88, indicating a much better fit for the data.

We also fit a separate spectral index for just the PWN. This fit has many fewer data points, as the PWN can only be resolved in the highest-resolution radio images (see Table 1). For this fit, we also exclude the 5500 and 9000 MHz data points, as these are outliers to the fit and disagree with the combined ATCA and Parkes data at similar frequencies, similar to the argument above. This is also shown by the reduced χ^2 values which is 20.97 when these two points are included, and is 0.40 when they are excluded, indicating that their exclusion results in a much better fit for the data. The shell spectral index is calculated in a similar way, with the shell flux densities being calculated as the difference between the total and PWN flux densities. Similarly, the 5500 and 9000 MHz data points are excluded from the fit as they are outliers to the fit, with the reduced χ^2 value being 71.94 when they are included, and 0.55 when they are excluded.

These results are shown in Fig 5, where the fitted points are shown in blue (for the total), green (for the PWN), and purple (for the shell), and all the non-fitted points are shown in red. We calculate spectral index values of -0.60 ± 0.02 for the total, -0.16 ± 0.03 for the PWN, and -0.58 ± 0.04 for the shell. The total and shell spectral index values fall within the standard range for SNRs within the MC (Bozzetto et al. 2017, Cotton et al. 2024) and are as expected for an SNR predominantly composed of a synchrotron emitting shell. The PWN spectral index value is flat, as expected for a PWN (Reynolds et al. 2017). These values differ from previous spectral index values calculated (Klinger et al. 2002), and this is likely due to the inclusion of more data points than previous estimates, which were obtained from archival radio observations of the LMC. Additionally, as we found that the ATCA points significantly disagreed with the combined ATCA and Parkes data, the inclusion of these outlying points likely impacted the previously calculated values.

3.4. Surface Brightness

We calculate the radio surface brightness as $\Sigma = S_{1\,\rm GHz}/\Omega$ where $\Sigma = S_{1\,\rm GHz}$ is the flux density at 1 GHz (for the shell component), calculated using the measured shell spectral index, and Ω is the angular area of the source, as defined in Section 3.1. We use the shell flux density and spectral index measurements so as to exclude any potential PWN contribution and allow a more consistent comparison with other SNRs. We calculate a surface brightness of $1.3{\times}10^{-21}\,\rm W\,m^{-2}\,Hz^{-1}$. We compare these values with the Σ-D distribution of Pavlović et al. (2018, their Fig. 3, our Fig. 6) and find that Goat's Eye falls within the typical distribution for SNRs.

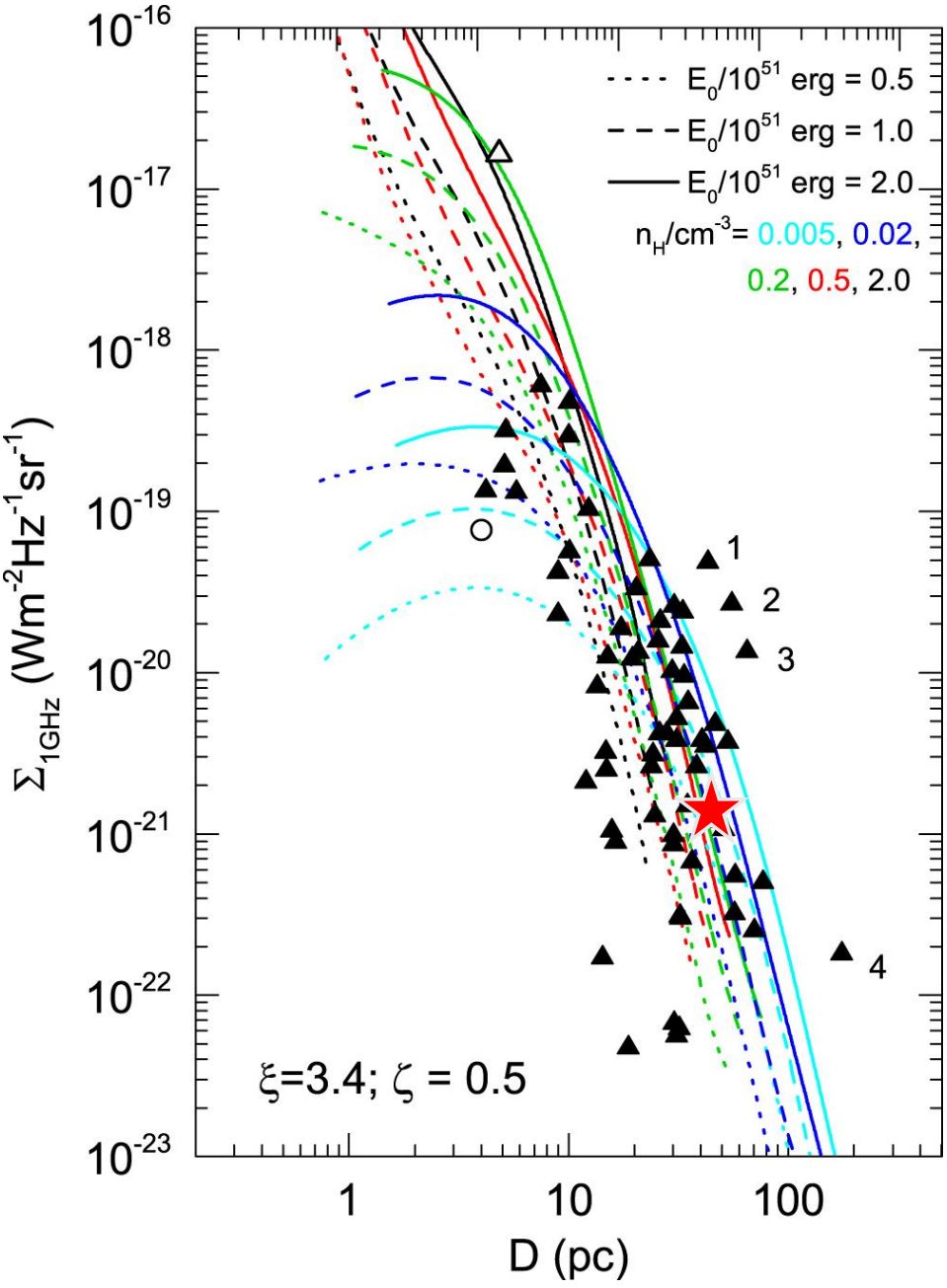

Fig. 6: Radio surface brightness to diameter diagram for SNRs at frequency $\nu = 1$ GHz, adopted from Pavlović et al. (2018, their fig. 3), shown as black triangles. Different line colours represent different ambient densities, while different line types represent different explosion energies. The open circle is young Galactic SNR G1.9+0.3 (Luken et al. 2020), and the open triangle represents Cassiopeia A. The numbers represent SNRs (1): CTB 37A, (2): Kes 97, (3): CTB 37B, and (4): G65.1+0.6. The red star represents Goat's Eye at estimated surface brightness of 1.3×10^{-21} W m^{-1} Hz^{-2} sr^{-1} and diameter of 45 pc (the diameter is taken as the major axis). The image shows evolutionary tracks for representative cases with injection parameter $\xi = 3.4$ and nonlinear magnetic field damping parameter $\zeta = 0.5$.

3.5. Polarisation

The ATCA observations consisted of Stokes Q and U observations, allowing us to measure the linear polarisation, rotation measure, and magnetic field of the PWN. Due to the lower surface brightness of the SNR shell, we were unable to accurately measure the shell's polarisation properties; however, we obtained polarisation measurements for the brighter PWN feature.

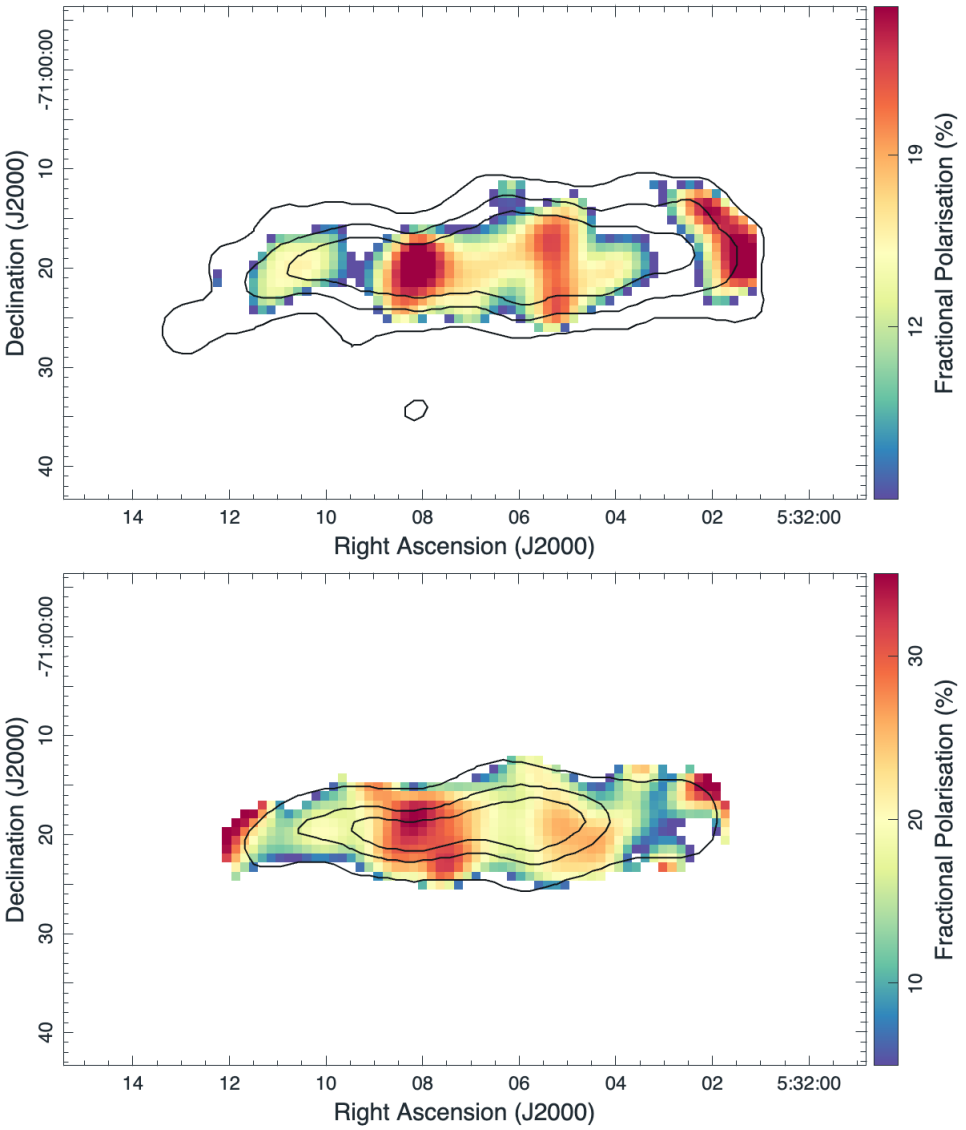

Fig. 7: Fractional polarisation images of Goat's Eye PWN overlaid with total intensity contours. **Top:** 5500 MHz fractional polarisation ATCA image with 5500 MHz Stokes I contours at levels of 0.2, 0.4, and 0.6 mJy beam^{-1}. **Bottom:** 9000 MHz fractional polarisation ATCA image with 9000 MHz Stokes I contours at levels of 0.2, 0.4, and 0.5 mJy beam^{-1}.

All images were convolved to a common beam size of $5'' \times 5''$ to minimise noise, and then the MIRIAD task IMPOL was used to generate the polarised intensity, fractional polarisation, and rotation measure images (see Figs. 7 and 8). The measured rotation measure was then used to de-rotate the polarisation vectors to map the electric field vectors, and these were then rotated by 90° to show the intrinsic magnetic field (see Fig. 8).

The linear PWN feature is visible in both polarisation maps with two areas of higher fractional polarisation in the centre and fading towards the edges. We measure an average fractional polarisation of $3.0 \pm 1.0\%$ with a peak of $9.0 \pm 1.0\%$ at 5.5 GHz and an average of $3.5 \pm 2.0\%$ with a peak of $26 \pm 6\%$ at 9 GHz. The rotation measure shows positive values ranging from $\sim$200$-$800 rad m^{-2}, with the highest value observed on the eastern tip. This corresponds approximately with the location of the X-ray source (Williams et al. 2005). This may represent the area of a hidden pulsar; however, if this is the case, we would also expect to see a higher fractional polarisation in this area.

3.6. Magnetic Field

We observe a highly ordered magnetic field oriented along the linear axis, similar to the results of

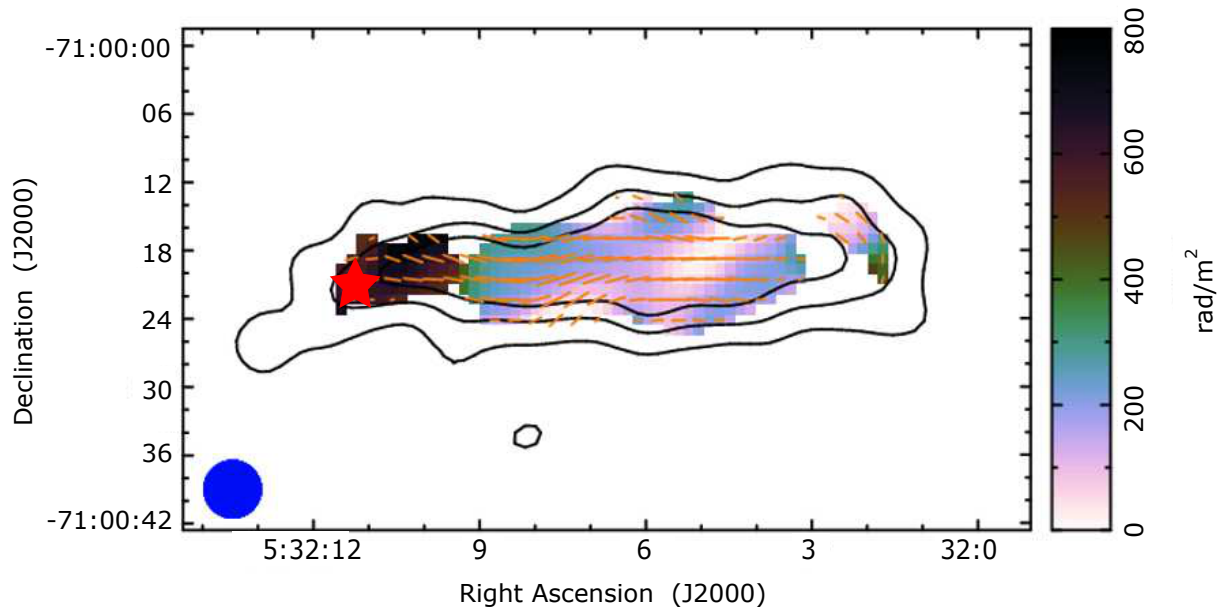

Fig. 8: *RM* map calculated between the observations at 5500 MHz and 9000 MHz with overlaid vectors in B-field direction, corrected for Faraday rotation. The contour lines are from intensity image at 5500 MHz at levels of 0.2, 0.4, and 0.6 mJy beam^{-1}. The red star indicates the location of the X-ray point source.

Klinger et al. (2002). The "zig-zag"-like structure observed in the radio-continuum (see Sec. 3.1) is also present in the magnetic field structure, with the magnetic field following this pattern. This is expected if this emission represents the tail of a bow-shock PWN.

We use an available equipartition model[4] (Arbutina et al. 2012, 2013, Urošević et al. 2018) to estimate Goat's Eye's magnetic field. We use measured values of $\alpha = -0.60$, angular radius $\theta = 1\farcm5$, $S_{1\,\mathrm{GHz}} = 0.34$ Jy (interpolated from the EMU and MeerKAT flux density measurements, see Sec. 3.4), and assume a value of $f = 0.25$. We find an average magnetic field of $B = 28.6\,\mu$G and a minimum energy of $E_{\mathrm{min}} = 2.3\times10^{49}$ ergs when assuming electron equipartition, and values of $B = 66.3\,\mu$G and $E_{\mathrm{min}} = 1.3\times10^{50}$ ergs for ion equipartition.

3.7. "Zig-zag" pulsar-wind nebula

The radio-continuum data presented here are consistent with a bow-shock PWN scenario. The region exhibits bright radio-continuum emission, accompanied by a flatter radio spectral index, which is consistent with enhanced particle acceleration at this location due to the constant energy input from an energetic pulsar. Similarly, the measured polarisation and ordered magnetic field traces the pulsar's path as it travels supersonically through the SNR interior and generates a bow-shock PWN behind it. In this scenario, the pulsar would likely be located at the eastern tip of the PWN with the tail leading back to the geometric centre of the SNR.

[4] http://poincare.matf.bg.ac.rs/~arbo/eqp

We observe a "zig-zag"-like structure in the PWN which was unseen in previous observations, and has not been observed in other known PWN structures. This structure is present in both radio-continuum (see Fig. 2, top inset) and in the magnetic field vector map (see Fig. 8). The fact that it is seen in the radio-continuum images, polarisation images, and the magnetic field indicates that it is an intrinsic physical structure. The zig-zag structure observed corresponds with the brighter areas of polarised emission, which appear almost as polarisation hotspots.

There are several physical mechanisms which can cause asymmetries or "knot-like" structures within highly magnetised plasma structures such as PWN. Some of these scenarios could include the formation of kinks, which can appear in some magnetised jets as unstable knots driven by areas of different compression or magnetic instabilities (Porth et al. 2013, Bromberg et al. 2019). Additionally, such a structure may be the result of the PWN travelling through the inner SN ejecta. Density inhomogeneities within the ejecta may deflect the PWN at different points, generating enhanced emission or general asymmetries. Additionally, the pulsar's proper motion may play a part in the structure, for example, if there is significant orbital motion or precession in its motion, then this may generate a "corkscrew"-like structure. These scenarios are possibilities, and the parameters cannot be constrained until the host pulsar is discovered.

Another interesting property of the PWN is that its direction appears to be aligned with one of the "ear"-like structures on the eastern side. This is potentially further supported by the HI analysis, where

the $p-v$ diagram shows a smaller cavity coincident with the PWN structure. We emphasise that this is not a definitive detection however, as the PWN size is at the same spatial scale as the HI data resolution, but there is an indication of a possible expanding structure. Therefore, the pulsar may be pushing out of the SNR shell, contributing to the observed "ear" blowout structure. Additionally, there are some recent theoretical models (Chiotellis et al. 2021), which suggest that SNR ears may be formed when the SNR forward shock interacts with a bipolar circumstellar medium.

Without further data, all these scenarios are speculative and future observations would be required. What can be seen from the observations is that this zig-zag structure is present, and the most likely cause is some form of asymmetry, interaction, or PWN dynamics. Our future high-sensitivity and resolution studies will focus further on this structure to determine its physical origin.

4. CONCLUSIONS

We have conducted radio-continuum observations and analysis of the LMC SNR N206, which we have nicknamed "Goat's Eye" due to the peculiar morphology of its PWN. We have focused on the bright PWN structure in the east. Specifically, we have calculated a spectral index for the total SNR and for the PWN, finding a steep ($\alpha = -0.60$) for the total and flat ($\alpha = -0.16$) for the PWN. These differ from previous spectral index values, likely due to our inclusion of several more data points from archival radio images. This greatly supports the scenario of a typical synchrotron SNR shell, with an interior PWN with more efficient particle acceleration.

The PWN was previously reported as a linear feature; the new observations reveal an unusual "zig-zag" structure, visible in both radio-continuum total intensity images, radio polarisation images, and in the magnetic field structure. The current data do not provide a sufficient explanation for the origin of this structure, but future observations will enable us to better constrain its nature and further our understanding of PWN dynamic structures.

Acknowledgements – The MeerKAT telescope is operated by the South African Radio Astronomy Observatory, which is a facility of the National Research Foundation, an agency of the Department of Science and Innovation.

This scientific work uses data obtained from Inyarrimanha Ilgari Bundara / the Murchison Radio-astronomy Observatory. We acknowledge the Wajarri Yamaji People as the Traditional Owners and native title holders of the Observatory site. CSIRO's ASKAP radio telescope is part of the Australia Telescope National Facility[5]. Operation of ASKAP is funded by the Australian Government with support from the National Collaborative Research Infrastructure Strategy. ASKAP uses the resources of the Pawsey Supercomputing Research Centre. Establishment of ASKAP, Inyarrimanha Ilgari Bundara, the CSIRO Murchison Radio-astronomy Observatory and the Pawsey Supercomputing Research Centre are initiatives of the Australian Government, with support from the Government of Western Australia and the Science and Industry Endowment Fund.

Support for the operation of the MWA is provided by the Australian Government (NCRIS), under a contract to Curtin University administered by Astronomy Australia Limited.

[5] http://www.atnf.csiro.au

REFERENCES

Alsaberi, R. Z. E., Maitra, C., Filipović, M. D., et al. 2019, MNRAS, 486, 2507
Alsaberi, R. Z. E., Filipović, M. D., Sano, H., et al. 2025, PASA, 42, e069
Arbutina, B., Urošević, D., Andjelić, M. M., Pavlović, M. Z. and Vukotić, B. 2012, ApJ, 746, 79
Arbutina, B., Urošević, D., Vučetić, M. M., Pavlović, M. Z. and Vukotić, B. 2013, ApJ, 777, 31
Asher, A. D., Smeaton, Z. J., Filipović, M. D., et al. 2025, PASA, 42, 111
Bordiu, C., Filipović, M. D., Umana, G., et al. 2024, A&A, 690, A53
Bozzetto, L. M. and Filipović, M. D. 2014, Ap&SS, 351, 207
Bozzetto, L. M., Filipovic, M. D., Crawford, E. J., De Horta, A. Y. and Stupar, M. 2012, SerAJ, 184, 69
Bozzetto, L. M., Filipovic, M. D., Haberl, F., et al. 2015, Publication of Korean Astronomical Society, 30, 149
Bozzetto, L. M., Filipović, M. D., Vukotić, B., et al. 2017, ApJS, 230, 2
Bozzetto, L. M., Filipović, M. D., Sano, H., et al. 2023, MNRAS, 518, 2574
Bradley, A., Smeaton, Z., Tothill, N., et al. 2025, PASA, 42, e032
Brantseg, T., McEntaffer, R. L., Bozzetto, L. M., Filipovic, M. and Grieves, N. 2014, ApJ, 780, 50
Bromberg, O., Singh, C. B., Davelaar, J. and Philippov, A. A. 2019, ApJ, 884, 39
Burger-Scheidlin, C., Brose, R., Mackey, J., et al. 2024, A&A, 684, A150
Camilo, F., Manchester, R. N., Gaensler, B. M. and Lorimer, D. R. 2002, ApJL, 579, L25
Chiotellis, A., Boumis, P. and Spetsieri, Z. T. 2021, MNRAS, 502, 176
Comrie, A., Wang, K.-S., Hsu, S.-C., et al. 2018, CARTA: The Cube Analysis and Rendering Tool for Astronomy
Cotton, W. D., Filipović, M. D., Camilo, F., et al. 2024, MNRAS, 529, 2443
Crawford, E. J., Filipović, M. D., de Horta, A. Y., Stootman, F. H. and Payne, J. L. 2008, SerAJ, 177, 61
Dickel, J. R., McIntyre, V. J., Gruendl, R. A. and Milne, D. K. 2005, AJ, 129, 790
Dimaratos, A., Cormier, D., Bigiel, F. and Madden, S. C.

2015, A&A, 580, A135
Filipović, M. D. and Tothill, N. F. H. 2021, Principles of Multimessenger Astronomy, AAS-IOP astronomy (Institute of Physics Publishing)
Filipović, M. D., Haynes, R. F., White, G. L., et al. 1995, A&AS, 111, 311
Filipovic, M. D., White, G. L., Jones, P. A., et al. 1996, in Astronomical Society of the Pacific Conference Series, Vol. 112, The History of the Milky Way and Its Satellite System, ed. A. Burkert, D. H. Hartmann and S. A. Majewski, 91
Filipović, M. D., Haynes, R. F., White, G. L. and Jones, P. A. 1998, A&AS, 130, 421
Filipović, M. D., Bojičić, I. S., Grieve, K. R., et al. 2021, MNRAS, 507, 2885
Filipović, M. D., Payne, J. L., Alsaberi, R. Z. E., et al. 2022, MNRAS, 512, 265
Filipović, M. D., Dai, S., Arbutina, B., et al. 2023, AJ, 166, 149
Filipović, M. D., Lazarević, S., Araya, M., et al. 2024, PASA, 41, e112
Filipović, M. D., Smeaton, Z. J., Bradley, A. C., et al. 2025a, ApJL, 984, L52
Filipovic, M. D., Smeaton, Z. J., Kothes, R., et al. 2025b, PASA, 42, e104
For, B.-Q., Staveley-Smith, L., Hurley-Walker, N., et al. 2018, MNRAS, 480, 2743
Fukui, Y., Aruga, M., Sano, H., et al. 2024, ApJ, 961, 162
Ghavam, M., Filipović, M. D., Alsaberi, R., et al. 2024, PASA, 41, e089
Gooch, R. 1995, in Astronomical Society of the Pacific Conference Series, Vol. 77, Astronomical Data Analysis Software and Systems IV, ed. R. A. Shaw, H. E. Payne and J. J. E. Hayes, 144
Gorjian, V., Werner, M. W., Mould, J. R., et al. 2004, ApJS, 154, 275
Guzman, J., Whiting, M., Voronkov, M., et al. 2019, ASKAPsoft: ASKAP science data processor software
Haberl, F. 2014, in The X-ray Universe 2014, ed. J.-U. Ness, 4
Haberl, F., Filipović, M. D., Bozzetto, L. M., et al. 2012, A&A, 543, A154
Hales, C. A., Gaensler, B. M., Chatterjee, S., van der Swaluw, E. and Camilo, F. 2009, ApJ, 706, 1316
Henize, K. G. 1956, ApJS, 2, 315
Hopkins, A., Kapinska, A., Marvil, J., et al. 2025, PASA, 42, e071
Hughes, A., Staveley-Smith, L., Kim, S., Wolleben, M. and Filipović, M. 2007, MNRAS, 382, 543
Hurley-Walker, N., Callingham, J. R., Hancock, P. J., et al. 2017, MNRAS, 464, 1146
Hurley-Walker, N., Gaensler, B. M., Leahy, D. A., et al. 2019, PASA, 36, e048
Kavanagh, P. J., Sasaki, M. and Points, S. D. 2012, A&A, 547, A19
Kim, S., Staveley-Smith, L., Dopita, M. A., et al. 2003, ApJS, 148, 473
Klinger, R. J., Dickel, J. R., Fields, B. D. and Milne, D. K. 2002, AJ, 124, 2135
Kothes, R., Reich, P., Foster, T. J. and Reich, W. 2017, A&A, 597, A116
Lakićević, M., van Loon, J. T., Meixner, M., et al. 2015, ApJ, 799, 50
Lasker, B. M. 1977, PASP, 89, 474
Lazarević, S., Filipović, M. D., Dai, S., et al. 2024a, PASA, 41, e032
Lazarević, S., Filipović, M. D., Koribalski, B. S., et al. 2024b, Research Notes of the AAS, 8, 107
Lazendic, J. S., Dickel, J. R., Haynes, R. F., Jones, P. A. and White, G. L. 2000, ApJ, 540, 808
Leahy, D. A. 2017, ApJ, 837, 36
Leahy, D. A., Ranasinghe, S., Hansen, J., Filipović, M. D. and Smeaton, Z. 2025, PASP, 137, 064502
Long, K. S., Helfand, D. J. and Grabelsky, D. A. 1981, ApJ, 248, 925
Lopez, L. A., Ramirez-Ruiz, E., Badenes, C., et al. 2009, ApJL, 706, L106
Lopez, L. A., Ramirez-Ruiz, E., Huppenkothen, D., Badenes, C. and Pooley, D. A. 2011, ApJ, 732, 114
Luken, K. J., Filipović, M. D., Maxted, N. I., et al. 2020, MNRAS, 492, 2606
Maggi, P., Haberl, F., Kavanagh, P. J., et al. 2016, A&A, 585, A162
Maggi, P., Filipović, M. D., Vukotić, B., et al. 2019, A&A, 631, A127
Maitra, C., Ballet, J., Filipović, M. D., et al. 2015, A&A, 584, A41
Maitra, C., Esposito, P., Tiengo, A., et al. 2021, MNRAS, 507, L1
Mathewson, D. S. and Clarke, J. N. 1973, ApJ, 180, 725
Mauch, T., Murphy, T., Buttery, H. J., et al. 2003, MNRAS, 342, 1117
McEntaffer, R. L., Brantseg, T. and Presley, M. 2012, ApJ, 756, 17
Meixner, M., Panuzzo, P., Roman-Duval, J., et al. 2013, AJ, 146, 62
Mills, B. Y., Turtle, A. J., Little, A. G. and Durdin, J. M. 1984, Australian Journal of Physics, 37, 321
Milne, D. K., Caswell, J. L. and Haynes, R. F. 1980, MNRAS, 191, 469
Owen, R. A., Filipović, M. D., Ballet, J., et al. 2011, A&A, 530, A132
Pavan, L., Bordas, P., Pühlhofer, G., et al. 2014a, A&A, 562, A122
Pavan, L., Bordas, P., Pühlhofer, G., et al. 2014b, in International Journal of Modern Physics Conference Series, Vol. 28, International Journal of Modern Physics Conference Series, 1460172
Pavan, L., Pühlhofer, G., Bordas, P., et al. 2016, A&A, 591, A91
Pavlović, M. Z., Urošević, D., Arbutina, B., et al. 2018, ApJ, 852, 84
Payne, J. L., White, G. L., Filipović, M. D. and Pannuti, T. G. 2007, MNRAS, 376, 1793
Payne, J. L., White, G. L. and Filipović, M. D. 2008, MNRAS, 383, 1175
Pennock, C. M., van Loon, J. T., Filipović, M. D., et al. 2021, MNRAS, 506, 3540

Pietrzyński, G., Graczyk, D., Gallenne, A., et al. 2019, Natur, 567, 200
Points, S. D., Long, K. S., Blair, W. P., et al. 2024, ApJ, 974, 70
Porth, O., Komissarov, S. S. and Keppens, R. 2013, MNRAS, 431, L48
Ranasinghe, S. and Leahy, D. 2019, Journal of High Energy Physics, Gravitation and Cosmology, 5, 907
Reid, W. A., Stupar, M., Bozzetto, L. M., Parker, Q. A. and Filipović, M. D. 2015, MNRAS, 454, 991
Reynolds, S. P., Pavlov, G. G., Kargaltsev, O., et al. 2017, SSRv, 207, 175
Rho, J. and Petre, R. 1998, ApJL, 503, L167
Sano, H., Suzuki, H., Nobukawa, K. K., et al. 2021, ApJ, 923, 15
Sano, H., Yamaguchi, H., Aruga, M., et al. 2022, ApJ, 933, 157
Sasaki, M., Zangrandi, F., Filipović, M., et al. 2025, A&A, 693, L15
Sault, R. J., Teuben, P. J. and Wright, M. C. H. 1995, in Astronomical Society of the Pacific Conference Series, Vol. 77, Astronomical Data Analysis Software and Systems IV, ed. R. A. Shaw, H. E. Payne and J. J. E. Hayes, 433
Smeaton, Z. J., Filipović, M. D., Koribalski, B. S., et al. 2024a, Research Notes of the AAS, 8, 158
Smeaton, Z. J., Filipović, M. D., Lazarević, S., et al. 2024b, MNRAS, 534, 2918
Smeaton, Z. J., Filipović, M. D., Alsaberi, R. Z. E., et al. 2025, arXiv:2506.15067
Smith, R. C. and MCELS Team. 1999, in IAU Symposium, Vol. 190, New Views of the Magellanic Clouds, ed. Y. H. Chu, N. Suntzeff, J. Hesser and D. Bohlender, 28
Tingay, S. J., Goeke, R., Bowman, J. D., et al. 2013, PASA, 30, e007
Urošević, D., Pavlović, M. Z. and Arbutina, B. 2018, ApJ, 855, 59
Velović, V., Filipović, M. D., Barnes, L., et al. 2022, MNRAS, 516, 1865
Velović, V., Cotton, W. D., Filipović, M. D., et al. 2023, MNRAS, 523, 1933
Virtanen, P., Gommers, R., Oliphant, T. E., et al. 2020, Nature Methods, 17, 261
Wayth, R. B., Lenc, E., Bell, M. E., et al. 2015, PASA, 32, e025
Williams, R. M. and Chu, Y. H. 2005, ApJ, 635, 1077
Williams, R. M., Chu, Y.-H., Dickel, J. R., et al. 1999, ApJS, 123, 467
Williams, R. M., Chu, Y.-H., Dickel, J., et al. 2005, ApJ, 628, 704
Xiao, L., Fürst, E., Reich, W. and Han, J. L. 2008, A&A, 482, 783
Yew, M., Filipović, M. D., Stupar, M., et al. 2021, MNRAS, 500, 2336
Yusef-Zadeh, F. and Bally, J. 1987, Natur, 330, 455
Zangrandi, F., Jurk, K., Sasaki, M., et al. 2024, A&A, 692, A237

МУЛТИФРЕКВЕНТНА РАДИО-КОНТИНУУМ СТУДИЈА ОСТАТКА СУПЕРНОВЕ У ВЕЛИКОМ МАГЕЛАНОВОМ ОБЛАКУ N206 (КОЗЈЕ ОКО) И "ЦИК-ЦАК" МАГЛИНА ПУЛСАРСКОГ ВЕТРА

M. Ghavam[1], Z. J. Smeaton[1], М. Д. Филиповић[1], R. Z. E. Alsaberi[2,1], C. Bordiu[3], W. D. Cotton[4,5], E. J. Crawford[1], A. M. Hopkins[6], R. Kothes[7], С. Лазаревић[1], D. Leahy[8], N. Rajabpour[1], S. Ranasinghe[8], G. P. Rowell[9], H. Sano[2], M. Sasaki[10], D. Shobhana[1], K. Tsuge[2,11], Д. Урошевић[12] and N. F. H. Tothill[1]

[1] *Western Sydney University, Locked Bag 1797, Penrith South DC, NSW 2751, Australia*
E–mail: *19594271@student.westernsydney.edu.au*

[2] *Faculty of Engineering, Gifu University, 1-1 Yanagido, Gifu 501-1193, Japan*

[3] *INAF-Osservatorio Astrofisico di Catania, Via Santa Sofía 78, I-95123 Catania, Italy*

[4] *National Radio Astronomy Observatory, 520 Edgemont Road, Charlottesville, VA 22903, USA*

[5] *South African Radio Astronomy Observatory Liesbeek House, River Park, Gloucester Road Cape Town, 7700, South Africa*

[6] *School of Mathematical and Physical Sciences, 12 Wally's Walk, Macquarie University, NSW 2109, Australia*

[7] *Dominion Radio Astrophysical Observatory, Herzberg Astronomy & Astrophysics, National Research Council Canada, P.O. Box 248, Penticton*

[8] *Department of Physics and Astronomy, University of Calgary, Calgary, Alberta, T2N IN4, Canada*

[9] *School of Physics, Chemistry and Earth Sciences, The University of Adelaide, Adelaide, 5005, Australia*

[10] *Dr Karl Remeis Observatory, Erlangen Centre for Astroparticle Physics, Friedrich-Alexander-Universität Erlangen-Nürnberg, Sternwartstraße 7, 96049 Bamberg, Germany*

[11] *Institute for Advanced Study, Gifu University, 1-1 Yanagido, Gifu 501-1193, Japan*

[12] *Катедра за астрономију, Математички факултет, Универзитет у Београду, Студентски трг 16, 11000 Београд, Србија*

УДК 524.354.4
Оригинални научни рад

Представљамо нова радио-континуум посматрања остатка супернове (ОСН) N206 у Великом Магелановом облаку (ВМО) коме смо дали надимак "Козје Око". Козје Око садржи унутрашњу радио структуру која је вероватно маглина пулсарског ветра (МПВ), коју детаљно анализирамо. Користимо нова радио-континуум посматрања са Аустралијског Телескопа Компактног Низа (АТКН), као и неколико архивских радио посматрања за израчунавање спектралног индекса. Нашли смо стрми спектрални индекс за цео ОСН ($\alpha = -0.60 \pm 0.02$), и раван спектрални индекс за МПВ ($\alpha = -0.16 \pm 0.03$). Такође меримо поларизацију и својства магнетног поља МПВ. Раније предложено као линеарна структура, нова посматрања показују необичну "цик-цак" структуру, видљиву ексклузивно у радио-континууму укључујући и линеарну поларизацију, и оријентацију магнетног поља. Порекло ове "цик-цак" структуре је и даље нејасно, али предлажемо један од могућих сценарија који захтева нова посматрања.